Available online at www.sciencedirect.com
ScienceDirect
Polymer 48 (2007) 7385–7392
polymer
www.elsevier.com/locate/polymer

In situ SAXS analysis of extended-chain crystallization during melt-drawing of ultra-high molecular weight polyethylene

Masaki Kakiage [a,1], Miho Sekiya [a], Takeshi Yamanobe [a], Tadashi Komoto [a], Sono Sasaki [b], Syozo Murakami [c], Hiroki Uehara [a,*]

[a] *Department of Chemistry, Gunma University, Kiryu, Gunma 376-8515, Japan*
[b] *Japan Synchrotron Radiation Research Institute, Sayo, Hyogo 679-5198, Japan*
[c] *Heian Jogakuin University, Takatsuki, Osaka 569-1092, Japan*

Received 1 May 2007; received in revised form 26 September 2007; accepted 7 October 2007
Available online 22 October 2007

Abstract

Phase development during melt-drawing of ultra-high molecular weight polyethylene (UHMW-PE) was analyzed by *in situ* small-angle X-ray scattering measurements using synchrotron radiation at the SPring-8. Films with different entanglement characteristics were prepared by solution blending of higher and lower MW samples with a viscosity average MW of 1.07×10^7 (higher) and 1.73×10^6 (lower), followed by compression molding at 180 °C. Independent of blend ratio, the strong streak attributed to extended-chain crystals (ECCs) appeared on the equator at the beginning point of the plateau stress region in the stress profile, which was one of the characteristic features of melt-drawing. A series of detailed analyses of these streaks suggested that two components with different dimensions were formed during melt-drawing: one was a precursory ECC, and the other was a mature ECC. These two ECC components grew synchronously at the beginning point of the plateau stress region for both films, independent of the entanglement characteristics of the film. However, the time of this synchronized growth was longer for the film with the lower MW component than for the film containing only the higher MW component. The resultant morphologies of the melt-drawn samples observed by transmission electron microscopy also reflected these characteristics. These results demonstrate that molecular entanglement characteristics dominate the unique crystallization mechanism that forms ECCs with different dimensions during melt-drawing of UHMW-PE.

Keywords: Ultra-high molecular weight polyethylene; Melt-drawing; Extended-chain crystallization

1. Introduction

Ultra-high molecular weight polyethylene (UHMW-PE) can be drawn even from the molten state using its higher melt viscosity [1–4]. An extended-chain crystal (ECC) was developed during melt-drawing, and then a folded-chain crystal (FCC) was developed during the cooling process in the orientation state [1–4]. Consistent with such morphologies, differential scanning calorimetry (DSC) revealed double endotherms corresponding to the ECC and FCC meltings [1–4]. The resultant ultra-oriented melt-drawn samples exhibited excellent tensile modulus and strength, reflecting effective extended-chain crystallization during melt-drawing [1,3,4].

In situ wide-angle X-ray diffraction (WAXD) measurements using synchrotron radiation revealed that transient crystallization into a metastable hexagonal form occurred during oriented crystallization into a final orthorhombic form during melt-drawing of UHMW-PE [5,6]. Furthermore, this transient crystallization into the hexagonal form during melt-drawing was dominated by the entanglement characteristics, i.e., the average number of entanglements per chain of the sample films [7]. The hexagonal crystallization occurred in the early

* Corresponding author. Tel.: +81 277 30 1332; fax: +81 277 30 1333.
E-mail address: uehara@chem-bio.gunma-u.ac.jp (H. Uehara).
[1] Research Fellow of the Japan Society for the Promotion of Science.

0032-3861/$ - see front matter © 2007 Elsevier Ltd. All rights reserved.
doi:10.1016/j.polymer.2007.10.018

stage of draw for the entangled component. However, it accelerated again in the later stage of draw for the less entangled component. Since this hexagonal form is the same as that of the ECC obtained during high-pressure crystallization of PE [8–12], such entanglement characteristics influence not only molecular packing within the crystal system but also the higher-order structure of crystal arrangements of ECC and FCC morphologies.

However, the relationship between molecular entanglement characteristics and structural formation of ECC and FCC during melt-drawing has not been identified. Therefore, this study attempts to analyze the structural development by *in situ* small-angle X-ray scattering (SAXS) measurements. These results are also compared to those of previous WAXD measurements for the same sample sets [7].

One advantage of small-angle scattering lies in its ability to detect density or concentration fluctuation with periodicity above the nanometer scale, like ECC or FCC. Such higher-order phase structures are usually measured by small-angle neutron scattering [13–20] and SAXS measurements [21–24], which can be combined with other measurements, i.e., DSC [25–28], WAXD [26–44], infrared spectroscopy [38,45,46] and transmission electron microscopy (TEM) [30,47–49] for various samples. Recently, the longitudinal acoustic mode technique in Raman spectroscopy, which is localized on straight fragments of individual macromolecules, has also been used for analyzing similar higher-order phase structures [30,50–53]. Here, the phase structure for a sample size on the order of 10 Å or larger can be evaluated by these analyzing techniques. This is quite different from the features of WAXD measurement, which is good for the analysis of the chain-packing dimension on the molecular level with the crystals.

2. Experiment

2.1. Initial materials

Two kinds of UHMW-PE with different MWs but a narrower MW distribution (MWD) were supplied by Asahi Kasei Chemicals Co. They were prepared using the metallocene catalyst system with viscosity average MWs (M_v) of 1.07×10^7 and 1.73×10^6. Gel permeation chromatography (GPC) measurements were performed for these materials, but components with MWs over 10^7 are undetectable by the GPC method. Thus, accurate analysis of MWD was difficult, especially for the UHMW-PE with a higher M_v of 1.07×10^7.

2.2. Sample preparation

Two kinds of films with a different number of entanglements per chain were prepared with component ratios (wt%) of 100/0 and 50/50 for both the higher and lower M_v materials, which are listed in Table 1. Appropriate amounts of these UHMW-PEs, 0.2 wt%, were dissolved in *p*-xylene at the boiling point in a nitrogen gas flow. Antioxidants, 0.5 wt% (based on polymer) of both octadecyl 3-(3,5-di-*tert*-butyl-4-hydroxyphenyl)-propanoate and bis(2,4-di-*tert*-butylphenyl)pentaerythritol diphosphite, were added. A gel-like aggregation was precipitated by slow cooling to room temperature (RT), filtered into a mat, and then soaked in an excess amount of acetone for *p*-xylene exchange. The mats were dried at RT in a vacuum. The dried mats were compression-molded into films at 180 °C and 30 MPa for 10 min, followed by slow cooling to RT. Before this molding procedure, a 0.5 wt% acetone solution of the above-mentioned antioxidants was applied to the surface of the dried mats. The resultant film thickness was ~0.7 mm. Their crystallinities were always around 50%, independent of the blend ratios (see Table 1).

Table 1
Component percentage and DSC characteristics of each blended film

Film	Component ratio (wt%)		Crystallinity[a] (%)	T_m[a] (°C)
	Higher M_v	Lower M_v		
100/0	100	0	49	134.6
50/50	50	50	52	134.2

[a] Evaluated by DSC measurement.

2.3. Melt-drawing

The drawing specimen was cut from these compression-molded films in a dumbbell shape, with the straight region 4 mm wide and 12.5 mm long. All melt-drawings were made at 155 °C, well above the sample melting temperature (T_m) given in Table 1, by using a previously designed high-temperature extension device for *in situ* measurements [54,55]. A heating chamber of this extension device covered the straight region of the dumbbell specimen. Before drawing, the sample specimen was held at 155 °C for 5 min for temperature equilibration. The cross-head speed of drawing was always 24 mm/min. The stress during this melt-drawing process was recorded using a load cell (Kyowa Electronic Instruments Co., Ltd., LUR-A-50NSA1) installed in the extension device.

Prepared films and drawing conditions used in these *in situ* SAXS measurements were the same as those used in previous *in situ* WAXD measurements [7].

2.4. Measurements

A PerkinElmer Pyris 1 DSC was used for DSC measurements. Heating scans were preformed up to 180 °C at a rate of 10 °C/min in a nitrogen gas flow. The peak temperature of the melting endotherm was based on the sample T_m. The temperature and heat of fusion (ΔH_f) were calibrated using indium and tin standards. Crystallinities were calculated from ΔH_f, assuming the ΔH_f of perfect PE crystals to be 290 J/g [56]. *In situ* SAXS measurements were carried out during the melt-drawing process using synchrotron radiation at the BL40B2 beamline of SPring-8 (Japan Synchrotron Radiation Research Institute, Hyogo, Japan). An extension device [54,55] was installed in the beamline, and SAXS images were continuously recorded during the melt-drawing process on a cooling-type CCD camera (Hamamatsu Photonics K.K., C4880). The wavelength of the synchrotron beam was

1.54 Å. The exposure time for each pattern was 1.5 s with a time interval of 5.5 s for date storage. TEM observations of the films were made by a JEOL JEM-1200EX electron microscope operated at 80 kV. The samples were stained by RuO_4 vapor and embedded in an epoxy resin; this caused the amorphous phase to appear as a darker region in the image. The assembly was cut into thin sections 50 nm thick with a Reichert Ultracut S microtome for TEM observation.

3. Results and discussion

It was previously reported that melt-drawing of UHMW-PE results in a unique stress–strain behavior [2,3,5–7], i.e., a plateau stress phenomenon in the early stage of draw, which is sensitive to the entanglement characteristics of the film. This stress–strain behavior is closely related to the hexagonal crystallization behavior during melt-drawing estimated from *in situ* WAXD measurements [5–7]. Therefore, the stress profiles on *in situ* SAXS measurements examined in this study were recorded. The films with different entanglement characteristics were melt-drawn after isothermal holding for 5 min at 155 °C, which well exceeds the end tail of the DSC melting endotherms (140 °C). Corresponding changes in the *in situ* SAXS patterns made it possible to discuss the phase structural changes during melt-drawing.

Fig. 1 depicts the stress profile of the 100/0 film containing only the higher M_v component and the corresponding change in the *in situ* SAXS patterns recorded during drawing at 155 °C. The stress profile exhibits a plateau stress region, which is a feature of melt-drawing. SAXS patterns exhibit the appearance of the strong streak on the equator at the beginning point of the plateau stress region. A similar streak on the equator has also been observed during the PE crystallization process [32,35,41]. This streak could be attributed to ECCs arranged parallel to the oriented direction. In this case, rapid extended-chain crystallization proceeds at the beginning point of the plateau stress region. However, no meridional scattering was observed even on the further draw. It has been reported that folded-chain crystallization during cooling from oriented melt causes this type of meridional scattering [32,35,41]. However, these results indicate that only the extended-chain crystallization occurred during the melt-drawing at 155 °C.

The same *in situ* analysis was carried out for melt-drawing of the 50/50 film with the lower M_v component. Fig. 2 depicts the stress profile and the corresponding change in the *in situ* SAXS patterns recorded during melt-drawing of the 50/50 film. The stress profile exhibits the plateau stress region, which is similar to that of the 100/0 film, but its stress level is almost half that for the 100/0 film because of the lower M_v component. SAXS patterns exhibit the strong streak on the equator at the beginning point of the plateau stress region, which is also similar to that of the 100/0 film. These results suggest that the extended-chain crystallization at the beginning point of the plateau stress region is independent of the entanglement characteristics of the film. It should be noted that the existence of FCC was not confirmed, even on the further draw for this 50/50 film.

The line profiles along the equators were extracted to quantitatively analyze the extended-chain crystallization characterized by a streak. However, the scattering at the center region is restricted by the beam stopper, as seen in the SAXS pattern. Therefore, the appropriate dimensional range should be determined first for such analyses of the equatorial line profiles. Fig. 3 compares the equatorial line profiles of undrawn and drawn samples and for air scattering without sample setting. The scattering vector q ($q = (4\pi\sin\theta)/\lambda$, where 2θ is the scattering angle and λ is the wavelength) is plotted on the horizontal axis. In the profile for air scattering, the q range lower than 0.0065 $Å^{-1}$ is blocked by the beam stopper, which is the shaded region in Fig. 3. Therefore, the q range was estimated to exceed 0.0065 $Å^{-1}$.

The difference in extended-chain crystallization between the 100/0 and 50/50 films was characterized by the equatorial line profiles extracted from the series of *in situ* SAXS patterns in Figs. 1 and 2. The Lorentz correction into Iq^2 was made in

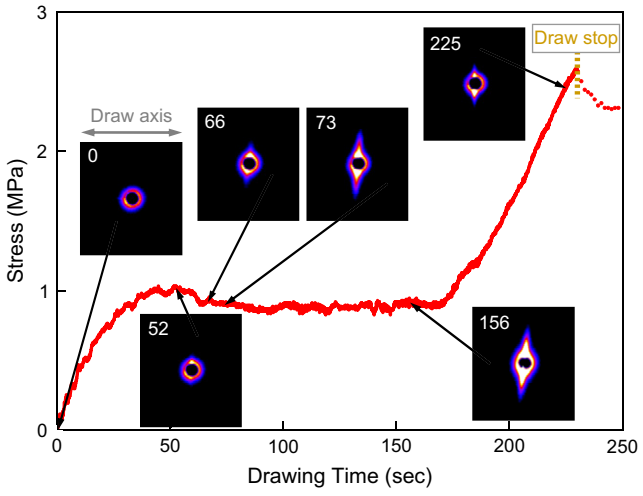

Fig. 1. Stress profile recorded at 155 °C with corresponding change of *in situ* SAXS patterns for 100/0 film. The draw direction for the SAXS patterns is horizontal. The drawing time in seconds is indicated for each pattern.

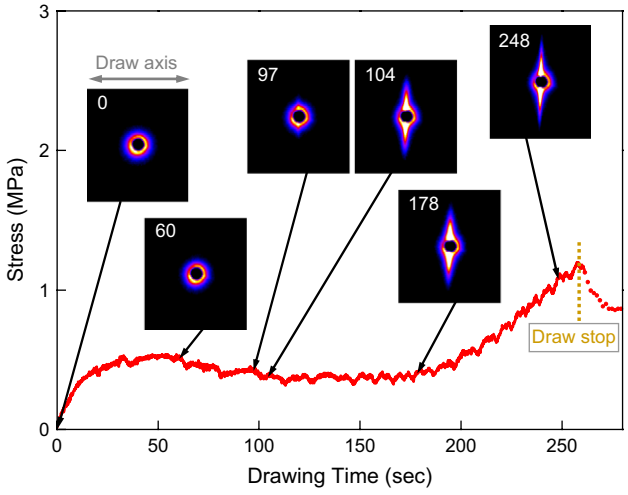

Fig. 2. Stress profile recorded at 155 °C with corresponding change of *in situ* SAXS patterns for 50/50 film.

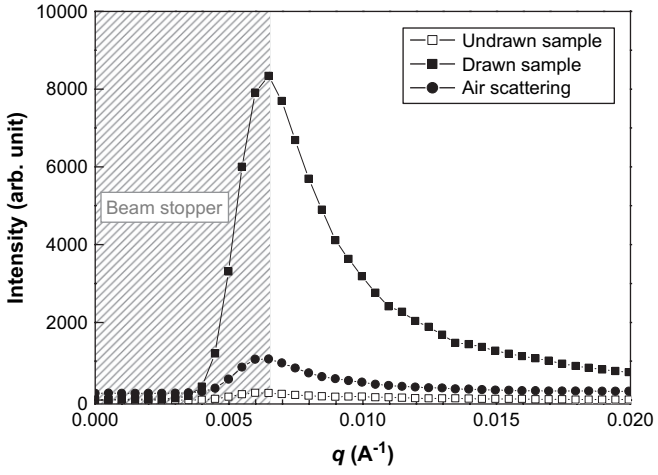

Fig. 3. SAXS line profiles extracted along the equator of the undrawn and drawn samples. The SAXS line profile of the air scattering is also plotted for comparison. The shaded area indicates the beam stopper region.

all equatorial line profiles [57], which makes it possible to evaluate the periodicity through the width direction of ECCs. The obtained line profiles for the 100/0 and 50/50 films were plotted as a function of drawing time in Figs. 4 and 5. In the case of the 100/0 film, the date in the time region beyond approximately 150 s was excluded from the following analyses because the detectable intensity for the CCD camera was exceeded by an unexpected increase in scattering intensity, which made the quantitative analysis difficult in this time region. For the 100/0 film, the rapid increase in intensity with the appearance of the streak is recognized at the beginning point of the plateau stress region, designated by a red line in Fig. 4. Beyond this critical drawing time, two peaks

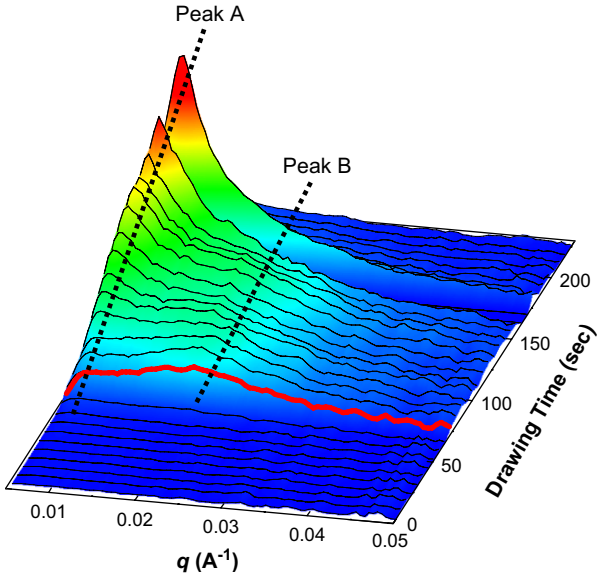

Fig. 4. 3-D plot of Lorentz-corrected line profiles extracted along the equators of the series of *in situ* SAXS patterns recorded during melt-drawing of 100/0 film at 155 °C. The red line indicates the profile recorded at the beginning point of the plateau stress region. (For interpretation of the references to color in this figure legend, the reader is referred to the web version of this article.)

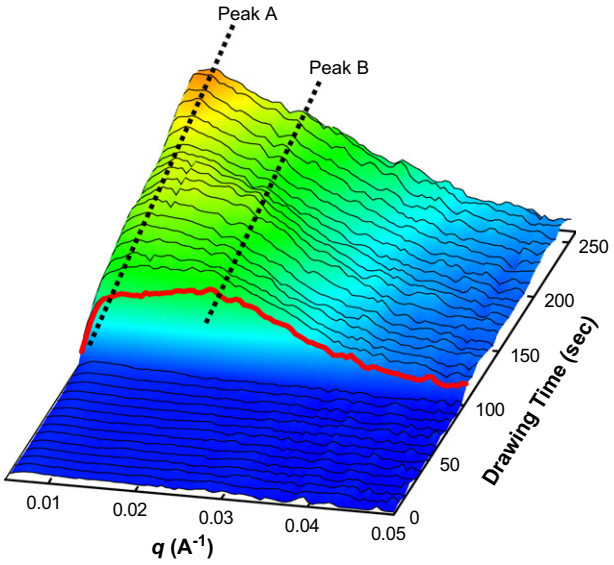

Fig. 5. 3-D plot of Lorentz-corrected line profiles extracted along the equators of the series of *in situ* SAXS patterns recorded during melt-drawing of 50/50 film at 155 °C. The meaning of the red line is the same as in Fig. 4. (For interpretation of the references to color in this figure legend, the reader is referred to the web version of this article.)

appeared. One peak was in the lower q range ($q \sim 0.008$ Å^{-1}), referred to as peak A in this study, and the other was a broad peak in a higher q range ($q \sim 0.02$ Å^{-1}), called peak B. For the 50/50 film, both the rapid increase in intensity and the appearance of the two peaks were similarly recognized beyond this critical drawing time, as shown in Fig. 5. These common features indicate that two ECC components with different dimensions were formed during melt-drawing for both films, independent of the entanglement characteristics of the film. Similar two peaks in the SAXS profile are observed for the PE during isothermal crystallization from the melt, which reflect the periodicity between stacked or isolated FCCs [45]. Under static condition, the sample prepared by blending of high-density and linear low-density PEs also exhibits such two peaks corresponding to the FCCs with different dimensions [25]. However, this melt-drawing is made at 155 °C, well above the equilibrium T_m of PE. Thus, FCC cannot exist for this process, i.e., only extended-chain crystallization occurs. Therefore, two peaks observed during melt-drawing process are attributed to the scattering between ECCs with different dimensions.

Meridional line profiles were also extracted from the series of *in situ* SAXS patterns in Figs. 1 and 2. However, evaluation of usual long period was difficult during melt-drawing, due to including disordered ECCs with mobile hexagonal form [7]. Additionally, no increase in intensity was observed for both films because folded-chain crystallization did not occur during melt-drawing, as described above.

The Lorentz-corrected intensity at each peak top was estimated from Figs. 4 and 5 in order to discuss the changes in these two ECC components during melt-drawing. The obtained peak intensities were plotted as a function of drawing time for the 100/0 and 50/50 films, given in Fig. 6a and b.

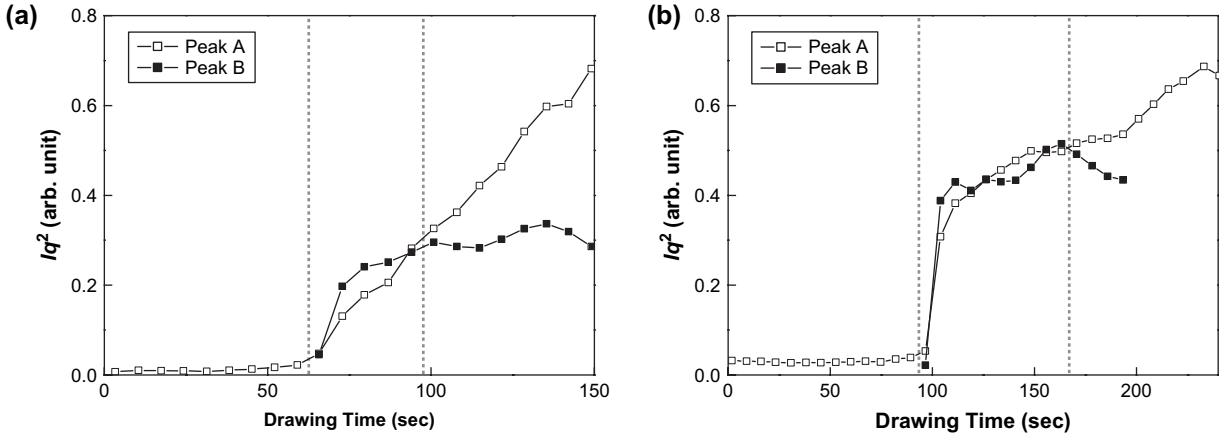

Fig. 6. Changes in Lorentz-corrected intensities at tops of peak A and peak B estimated from Figs. 4 and 5: (a) 100/0 film and (b) 50/50 film.

For the 100/0 film (Fig. 6a), only a minor change was observed before the beginning point of the plateau stress region. However, beyond this critical drawing time, the intensities of both peak A and peak B increase simultaneously. Even further beyond this time, only peak A continues to increase. Such a characteristic categorization is applicable during drawing for the 50/50 film (Fig. 6b). However, the length of synchronized growth region of peak A and peak B for the 50/50 film is far longer than that for the 100/0 film. Furthermore, the intensity of peak B is restricted beyond this synchronized growth region. It should be noted that peak B finally disappears in a later stage of the draw. Considering that peak B appears at the lower q range and has a smaller dimension, this component corresponds to a precursory ECC. In contrast, peak A increases throughout the entire draw for both films; thus it corresponds to a mature ECC grown from the precursory ECC.

Here, the result of previous *in situ* WAXD measurements confirmed that characteristic transient crystallization into the hexagonal form occurred at the beginning point of the plateau stress region during melt-drawing of UHMW-PE [7], where the conditions were the same as in this study. This transient crystallization behavior reflects the disentanglement of initial entangled melt. Thus, structural formation estimated from SAXS measurements and molecular entanglement characteristic estimated from WAXD measurements were compared and their correlations were discussed. Changes in peak intensities of the hexagonal (100) and orthorhombic (110) reflections for the 100/0 and 50/50 films during melt-drawing are summarized in Fig. 7a and b.

The SAXS results for the 100/0 film (Fig. 6a) demonstrate that synchronized growth of the precursory ECC corresponding to peak B and the mature ECC corresponding to peak A proceeds from the beginning point of the plateau stress region until 100 s. Beyond this synchronized growth region, the growth of precursory ECC is restricted and only mature ECC grows. In contrast, the WAXD analysis results (Fig. 7a) indicate that transient crystallization into the hexagonal form and rapid transition into orthorhombic form occur in a similar time region. These results indicate that synchronized growth estimated from SAXS analysis and transient crystallization estimated from WAXD analysis are closely correlated. Additionally, since both growths of precursory ECC and hexagonal form are restricted in the later stage of draw, this precursory ECC corresponds to the hexagonal form, which consists of disentangled chains. Therefore, transient growth into the precursory ECC with the hexagonal form proceeds at the early stage of draw. A similar comparison of SAXS and WAXD results was examined for the 50/50 film. SAXS analysis results

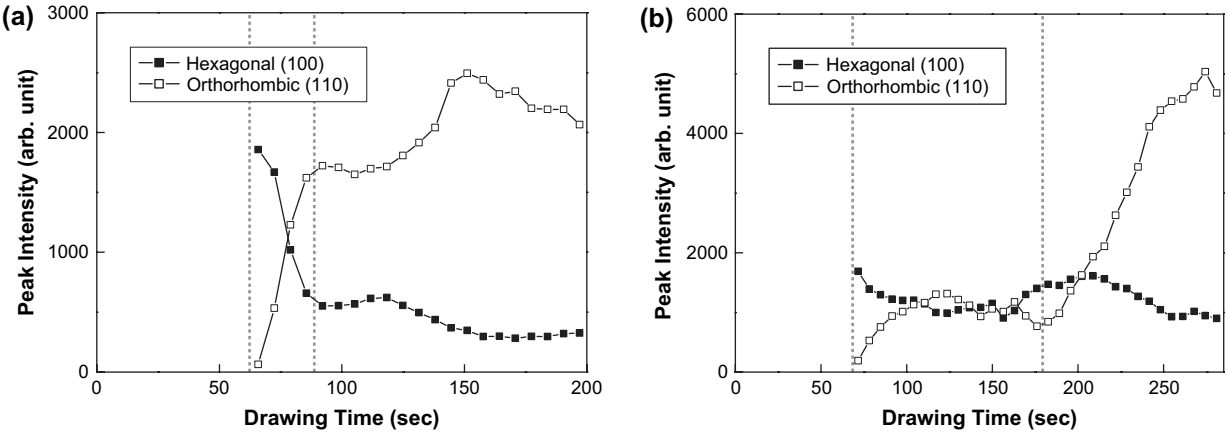

Fig. 7. Changes in peak intensities of the hexagonal (100) and orthorhombic (110) reflection peaks estimated from the data of previous *in situ* WAXD measurements during melt-drawing at 155 °C [7]: (a) 100/0 film and (b) 50/50 film.

(Fig. 6b) reveal that the synchronized growth region is far longer than that of the 100/0 film, which agrees with the remaining hexagonal form demonstrated by the WAXD analysis (Fig. 7b). With further draw, the precursory ECC decreases and finally disappears. This indicates the selective growth of the mature ECC at the later stage of draw. Here, in the WAXD analysis, a rapid increase of the orthorhombic form is observed in this time region. Therefore, the mature ECC could be attributed to the orthorhombic crystal. Furthermore, the disappearance of the precursory ECC in the later stage of draw indicates that the transformation from the precursory into mature ECCs is more accelerated with the oriented crystallization in this time region. Considering that this disappearance of the precursory ECC is observed only for this 50/50 film with the lower M_v component, the chain slippage during melt-drawing might accelerate the oriented crystallization in this time region for the 50/50 film, reflecting the lower entanglement density of the film [7].

The differences in morphologies of melt-drawn samples were also analyzed by TEM observation. Fig. 8 provides a series of TEM images for the 100/0 and 50/50 films: (a) undrawn, (b) melt-drawn at the beginning point of the plateau stress region and (c) in the later stage of draw. The latter two sets correspond to the categorizations of the synchronized growth and selective growth regions, which were estimated from the above *in situ* SAXS analysis given in Fig. 6. For both films, the initial morphology exhibits the homogeneous spherulitic structure consisting of FCCs (Fig. 8a). However, for the melt-drawn samples (Fig. 8b and c), the morphologies obtained for the 100/0 and 50/50 films are different. For the 100/0 film melt-drawn at the beginning point of the plateau stress region (Fig. 8b, left), the morphology combined the arranged crystalline structures along the draw direction and the lozenge crystalline blocks are observed. For the further drawn sample (Fig. 8c, left), the lozenge crystalline block grows along the draw direction while the arranged crystalline structure disappears. However, no four-point pattern attributed to the lozenge crystalline block was recognized in the *in situ* SAXS pattern recorded during melt-drawing, only the streak attributed to the ECCs appeared. Thus, this lozenge crystalline block must be formed by the sample reduction during cooling. Therefore, the lozenge crystalline block observed for the sample melt-drawn in the later stage of draw (Fig. 8c, left) corresponds to the mature ECC. In contrast, the arranged crystalline structure observed only at the beginning point of the plateau stress region (Fig. 8b, left) arises from the precursory ECC. This precursory ECC with a hexagonal form has more mobility than the mature ECC with stable orthorhombic form. Consequently, the orientation of the precursory ECC is maintained for the melt-drawn sample, due to effective releasing of retractive stress during cooling with ends fixed.

For the 50/50 film melt-drawn at the beginning point of the plateau stress region (Fig. 8b, right), the lozenge crystalline blocks are observed, similar to the 100/0 film. Furthermore, deficient oriented FCCs are also observed abundantly. Considering that the separation into the more and less entangled components proceeds before this time [7], these FCCs consist of

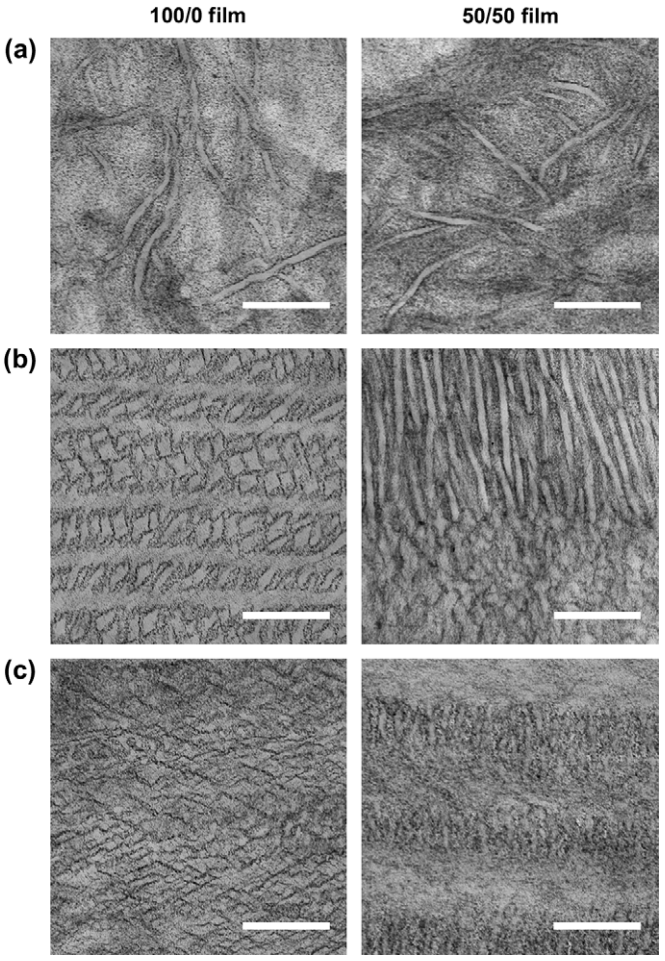

Fig. 8. Series of TEM images for the 100/0 (left) and 50/50 (right) films: (a) undrawn, (b) melt-drawn at the beginning point of the plateau stress region corresponding to the synchronized growth region of the precursory and mature ECCs and (c) in a later stage of draw corresponding to the selective growth region of the mature ECC. Draw direction for (b) and (c) is horizontal. All scale bars are 250 nm.

the lower M_v component that exists in the oriented amorphous during melt-drawing, followed by crystallization during cooling. For the further drawn sample (Fig. 8c, right), the morphology consisting of the longitudinal-oriented ECCs and the parallel-oriented FCCs appears, not the lozenge crystalline block like the 100/0 film (Fig. 8c, left). Here, the selective growth of the mature ECC is more accelerated in the later stage of draw only for the 50/50 film with the lower M_v component. Thus, oriented mature ECC with less entanglement survives as the longitudinal-oriented ECC after cooling. Furthermore, the parallel-oriented FCC (Fig. 8c, right) is thinner than the previous oriented FCC (Fig. 8b, right), due to crystallization from a more entangled state with a higher M_v component. These results indicate that molecular entanglement characteristics dominate the transformation from the precursory into mature ECCs during melt-drawing and the resultant morphologies of the melt-drawn samples of UHMW-PE.

Synchrotron X-ray analysis, which is a reciprocal space analysis, is preferred to perform *in situ* measurement because the quality of the time-resolved data improves for a good signal-

to-noise ratio with the Fourier transform. However, it is hard to imagine an actual structural change, not a real-space analysis. A complementary combination with TEM observation enables us to comprehensively understand the phase development mechanism with complicated behavior like this melt-drawing.

Recently, Rastogi et al. [58] note the effect of the entangled state of chains on static crystallization, i.e., a heterogeneous melt induces the earlier onset of folded-chain crystallization compared to the melt with a homogeneous distribution of entanglements. In contrast, extended-chain crystallization occurs through disentanglement of chains for our melt-drawing process. However, these behaviors would be combined by relaxation time of the chain. Namely, both of their cooling condition for static crystallization and our drawing condition for dynamic crystallization can vary the relaxation time, reflecting entanglement characteristics.

4. Conclusions

Phase development during melt-drawing of UHMW-PE was analyzed by *in situ* SAXS measurements using synchrotron radiation. Independent of entanglement characteristics of the film, the strong streak attributed to ECC appeared on the equator at the beginning point of the plateau stress region. However, no meridional scattering attributed to FCC was recognized in the features of the draw. Analyses of these streaks revealed that two ECC components with different dimensions, namely the precursory and mature ECCs, were formed during melt-drawing. For the film containing only the higher M_v component, both precursory and mature ECCs grew synchronously; then selective growth of the mature ECC proceeded. The former synchronized growth region corresponded to the transient crystallization region of the hexagonal form detected by previous WAXD measurements. This means that the precursory ECC has the hexagonal form. In contrast, this synchronized growth region in the film with the lower M_v component was far longer, reflecting the gentle crystal transition confirmed by WAXD measurements. Furthermore, later selective growth of the mature ECC was more accelerated in the later stage of draw, due to the oriented crystallization into the stable orthorhombic form. Therefore, the mature ECC could be attributed to the orthorhombic crystals. These differences in the growth mechanisms of the ECC obtained from these SAXS measurements were also realized in the resultant morphologies analyzed by TEM observation. These results demonstrate that molecular entanglement characteristics dominate the phase development mechanism of these different ECCs during melt-drawing of UHMW-PE.

Acknowledgements

In situ measurements using synchrotron radiation were performed at the BL40B2 in the SPring-8 with the approval of the Japan Synchrotron Radiation Research Institute (JASRI) (Proposal Nos. 2003B0303-NL2b-np/2003B0418-NL2b-np). We appreciate the cooperation of Dr. Katsuaki Inoue (JASRI). This work was partly supported by The Sumitomo Foundation and the Industrial Technology Research Grant Program in '04 from the New Energy and Industrial Technology Development Organization (NEDO) of Japan.

References

[1] Bashir Z, Keller A. Colloid Polym Sci 1989;267:116.
[2] Uehara H, Nakae M, Kanamoto T, Zachariades AE, Porter RS. Macromolecules 1999;32:2761.
[3] Nakae M, Uehara H, Kanamoto T, Ohama T, Porter RS. J Polym Sci Part B Polym Phys 1999;37:1921.
[4] Nakae M, Uehara H, Kanamoto T, Zachariades AE, Porter RS. Macromolecules 2000;33:2632.
[5] Uehara H, Kakiage M, Yamanobe T, Komoto T, Murakami S. Macromol Rapid Commun 2006;27:966.
[6] Kakiage M, Yamanobe T, Komoto T, Murakami S, Uehara H. J Polym Sci Part B Polym Phys 2006;44:2455.
[7] Kakiage M, Yamanobe T, Komoto T, Murakami S, Uehara H. Polymer 2006;47:8053.
[8] Wunderlich B, Arakawa T. J Polym Sci Part A 1964;2:3697.
[9] Bassett DC, Turner B. Nat Phys Sci 1972;240:146.
[10] Asahi T. J Polym Sci Polym Phys Ed 1984;22:175.
[11] Rastogi S, Kurelec L, Lemstra PJ. Macromolecules 1998;31:5022.
[12] Kurelec L, Rastogi S, Meier RJ, Lemstra PJ. Macromolecules 2000;33:5593.
[13] Sadler DM, Keller A. Macromolecules 1977;10:1128.
[14] Sadler DM, Keller A. Science 1979;203:263.
[15] Sadler DM, Barham PJ. J Polym Sci Polym Phys Ed 1983;21:309.
[16] Sadler DM, Barham PJ. Polymer 1990;31:36.
[17] Sadler DM, Barham PJ. Polymer 1990;31:43.
[18] Sadler DM, Barham PJ. Polymer 1990;31:46.
[19] Jinnai H, Hasegawa H, Hashimoto T, Han CC. J Chem Phys 1993;99:4845.
[20] Takeno H, Koizumi S, Hasegawa H, Hashimoto T. Macromolecules 1996;29:2440.
[21] Bellare A, Schnablegger H, Cohen RE. Macromolecules 1995;28:7585.
[22] Men Y, Rieger J, Homeyer J. Macromolecules 2004;37:9481.
[23] Polushkin E, Bondzic S, de Wit J, Alberda van Ekenstein G, Dolbnya I, Bras W, et al. Macromolecules 2005;38:1804.
[24] Okada K, Watanabe K, Wataoka I, Toda A, Sasaki S, Inoue K, et al. Polymer 2007;48:382.
[25] Zhao Y, Liu S, Yang D. Macromol Chem Phys 1997;198:1427.
[26] Abe S, Takahashi H. J Appl Crystallogr 2003;36:515.
[27] Shinohara Y, Kawasaki N, Ueno S, Kobayashi I, Nakajima M, Amemiya Y. Phys Rev Lett 2005;94:097801.
[28] Tashiro K, Tanaka R. Polymer 2006;47:5433.
[29] Cho MH, Kyu T, Lin J-S, Saijo K, Hasimoto T. Polymer 1992;33:4152.
[30] Rastogi S, Spoelstra AB, Goossens JGP, Lemstra PJ. Macromolecules 1997;30:7880.
[31] Butler MF, Donald AM. Macromolecules 1998;31:6234.
[32] Samon JM, Schultz JM, Hsiao BS, Seifert S, Stribeck N, Gurke I, et al. Macromolecules 1999;32:8121.
[33] Samon JM, Schultz JM, Hsiao BS. Polymer 2000;41:2169.
[34] Wang Z-G, Hsiao BS, Sirota EB, Srinivas S. Polymer 2000;41:8825.
[35] Schultz JM, Hsiao BS, Samon JM. Polymer 2000;41:8887.
[36] Wu J, Schultz JM, Samon JM, Pangelinan AB, Chuah HH. Polymer 2001;42:7161.
[37] Hama H, Tashiro K. Polymer 2003;44:2159.
[38] Hama H, Tashiro K. Polymer 2003;44:6973.
[39] Kawakami D, Hsiao BS, Burger C, Ran S, Avila-Orta C, Sics I, et al. Macromolecules 2005;38:91.
[40] Sakurai T, Nozue Y, Kasahara T, Mizunuma K, Yamaguchi N, Tashiro K, et al. Polymer 2005;46:8846.
[41] Keum JK, Somani RH, Zuo F, Burger C, Sics I, Hsiao BS, et al. Macromolecules 2005;38:5128.
[42] Kawakami D, Ran S, Burger C, Avila-Orta C, Sics I, Chu B, et al. Macromolecules 2006;39:2909.
[43] Ogino Y, Fukushima H, Takahashi N, Matsuba G, Nishida K, Kanaya T. Macromolecules 2006;39:7617.

[44] Konishi T, Nishida K, Kanaya T. Macromolecules 2006;39:8035.
[45] Sasaki S, Tashiro K, Kobayashi M, Izumi Y, Kobayashi K. Polymer 1999;40:7125.
[46] Hama H, Tashiro K. Polymer 2003;44:3107.
[47] Xu T, Hawker CJ, Russell TP. Macromolecules 2003;36:6178.
[48] Xu T, Hawker CJ, Russell TP. Macromolecules 2005;38:2802.
[49] Xu T, Zvelindovsky AV, Sevink GJA, Lyakhova KS, Jinnai H, Russell TP. Macromolecules 2005;38:10788.
[50] Kober K, Gorshkova IA, Savitsky AV, Tshmel AE. J Polym Sci Part B Polym Phys 1998;36:2829.
[51] Tsobkallo K, Vasilieva V, Khizhnyak S, Pakhomov P, Galitsyn V, Ruhl E, et al. Polymer 2003;44:1613.
[52] Pakhomov PM, Khizhnyak S, Reuter H, Galitsyn V, Tshmel A. Polymer 2003;44:4651.
[53] Tsobkallo K, Vasilieva V, Kakiage M, Uehara H, Tshmel A. J Macromol Sci Part B Phys 2006;45:407.
[54] Murakami S, Tanno K, Tsuji M, Kohjiya S. Bull Inst Chem Res Kyoto Univ 1995;72:418.
[55] Murakami S. Nippon Kagaku Kaishi 2000;2:141.
[56] Wunderlich B, Cormier CM. J Polym Sci Part A-2 1967;5:987.
[57] Strobl GR, Schneider M. J Polym Sci Polym Phys Ed 1980;18:1343.
[58] Lippits DR, Rastogi S, Hohne GWH, Mezari B, Magusin PCMM. Macromolecules 2007;40:1004.